Supporting Information

Ligand Exchange-Assisted Layer-by-Layer Assembly of Au–Pt Bimetallic Nanocomposite Films and their Electrocatalytic Activities for Hydrogen Evolution Reaction

Sujin Lee[1], Yongkwon Song[2,3], Jinhan Cho[3], Youn Jeong Jang[1], Bongjun Yeom[1]**

[1]Department of Chemical Engineering, Hanyang University,Seoul 04763, Republic of Korea

[2]Department of Materials Science and Engineering, Northwestern University, Evanston, IL 60208, USA

[3]Department of Chemical and Biological Engineering, Korea University,Seoul 02841, Republic of Korea

*Corresponding author; yjang53@hanyang.ac.kr, byeom@hanyang.ac.kr

Table S1. Inductively coupled plasma mass spectrometer (ICP-MS) analysis of Au20, Pt20, and AuPt10.

Sample	Element	Measured (ppm)	Mass fraction (%)
Au20	Au	1,950	-
Pt20	Pt	16.3	-
AuPt10	Au	1,650	99.27
	Pt	12.2	0.73

Table S2. Comparison of the HER activity in acidic electrolyte of Au-Pt catalyst with low amount Pt-based catalysts reported in literatures.

Catalyst	$\eta_{=10}$ (mV)	Tafel slope (mV dec^{-1})	Electrolyte	Synthesis method	Pt content
AuPt10 (This work)	95	52.4	0.5 M H_2SO_4	Ligand exchange-assisted Layer-by-Layer self-assembly	0.73 wt% (1.5 μg cm^{-2}) (/Au, Pt)
AuPt (Ref S1)	250	86	0.5 M H_2SO_4	Pulsed laser irradiation (PLI) & Ultrasonochemical process (USP)	–
C/Ni-AuPt-2 (Ref S1)	131	66	0.5 M H_2SO_4	Pulsed laser ablation (PLA)	11.83 wt% (/Au, Pt, C, N)
PtAuNPs/CNF (Ref S2)	235	84	0.5 M H_2SO_4	In situ reduction & electrospinning procedure	3.09 wt% (/Pt, Au, C)
Au@Pt NPs/rGO (Ref S3)	45	42	0.5 M H_2SO_4	One-pot co-reduction approach	74.91 wt% (/Au, Pt)
$Au_{33}Pt_{67}$ (Ref S4)	171	81	0.5 M H_2SO_4	Ultrasonication-assisted wet-chemical fabrication	67 wt% (/Au, Pt)
AgPt-tipped on Au NSs (Ref S5)	75	37	N_2-saturated 0.5 M H_2SO_4	Seed-mediated method	5.86 μg cm^{-2}
$Pt_{0.5}/Fe_2O_3$ (Ref S6)	221	135.8	0.5 M H_2SO_4	Thermally annealing process	0.70 wt% (/Pt, Fe, O, C, Cl)
Pt_{10}/Fe_2O_3 (Ref S6)	24	27.6	0.5 M H_2SO_4	Thermally annealing process	26.17 wt% (/Pt, Fe, O, C, Cl)
Pt-MoS_2 (Ref S7)	67.4	76.2	0.5 M H_2SO_4	Wet-chemical method	3.0 wt% (/Pt, Mo, S)
Pt@MoO_2/MoS_2 (Ref S8)	42	26.7	0.5 M H_2SO_4	Underpotential deposition (UPD)-replacement method	12.45 wt% (/Pt, Mo, O, S)
Pt–CoP (Ref S9)	53	28.2	Ar-saturated 0.5 M H_2SO_4	Chemical vapor deposition	1.09 wt% (/Pt, Co, P)

Table S3. Deconvolution of XPS Pt 4f peaks in TOA-PtNP, Pt20, and AuPt10.

Sample	Component	Peak position (eV)	Peak area (a.u.)
TOA-PtNP	Pt $4f_{7/2}$	72.08 (Pt^0)	3132.4
		73.08 (Pt^{2+})	3377.6
	Pt $4f_{5/2}$	75.38 (Pt^0)	3188.2
		76.43 (Pt^{2+})	1980.0
Pt20	Pt $4f_{7/2}$	71.16 (Pt^0)	7846.4
		72.33 (Pt^{2+})	24169.8
	Pt $4f_{5/2}$	74.46 (Pt^0)	5354.5
		75.61 (Pt^{2+})	19737.3
AuPt10	Pt $4f_{7/2}$	71.25 (Pt^0)	4813.5
		72.60 (Pt^{2+})	13828.2
	Pt $4f_{5/2}$	74.52 (Pt^0)	6945.2
		75.89 (Pt^{2+})	5872.5

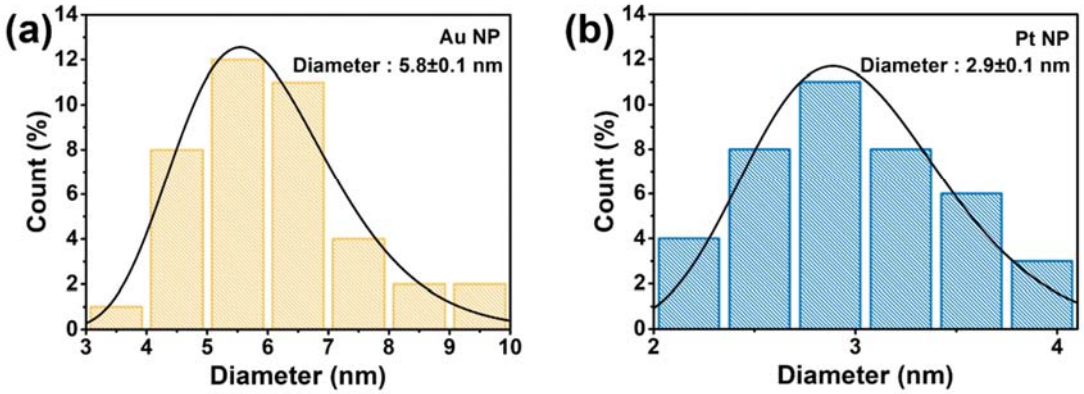

Figure S1. Typical TEM size distribution showing the particle diameter for (a) Au NPs and (b) Pt NPs. Average diameters were obtained from fittings of log-normal distributions.

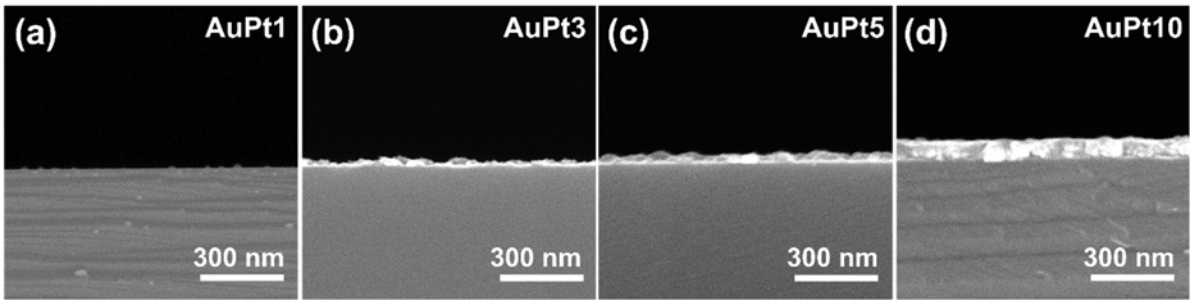

Figure S2. FE-SEM cross-sectional images of (a) AuPt1, (b) AuPt3, (c) AuPt5, and (d) AuPt10 samples.

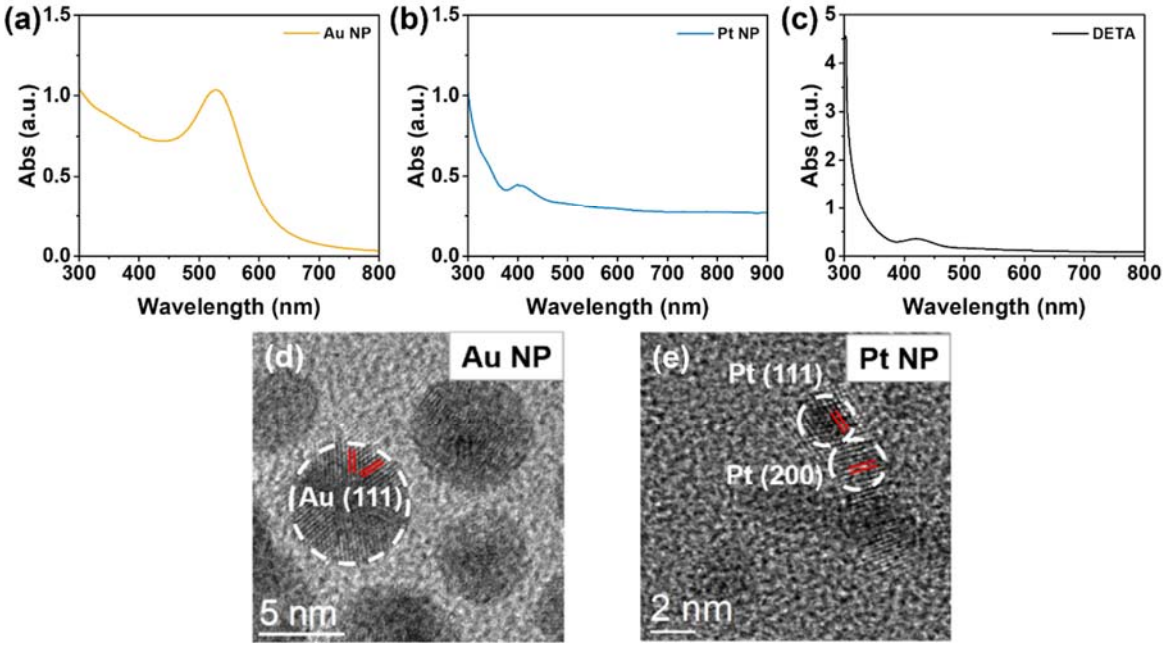

Figure S3. UV–visible spectra of (a) Au NPs, (b) Pt NPs, and (c) DETA. TEM images of (d) Au NPs and (e) Pt NPs.

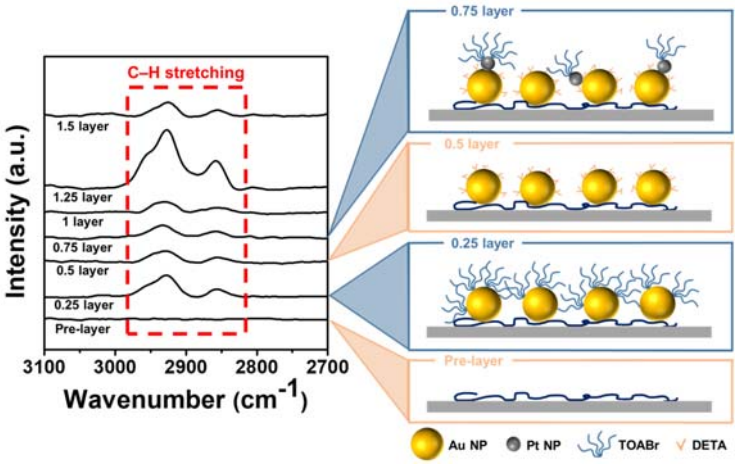

Figure S4. ATR−FTIR spectra and schematic images of (DETA/AuNP/DETA/PtNP)$_n$ multilayers as a function of the layer number (n).

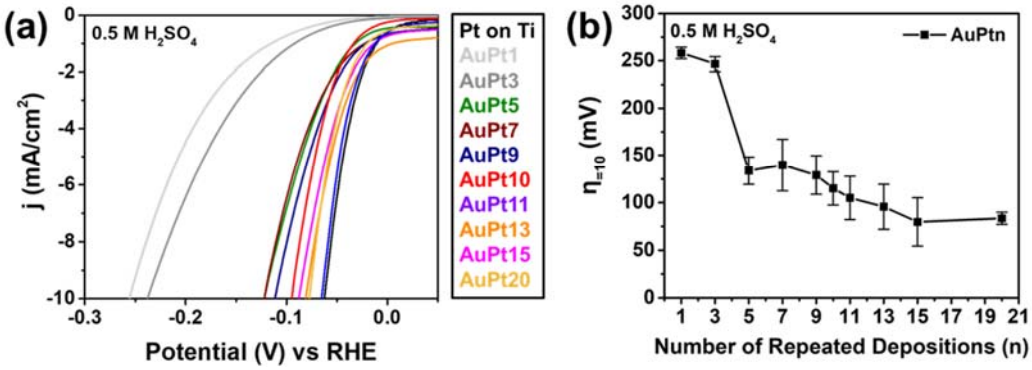

Figure S5. LSV polarization curves for AuPt*n* samples and Pt sputtered onto Ti (a) in 0.5 M H_2SO_4. (b) Overpotentials corresponding to the curves shown in (a) at 10 mA cm^{-1}.

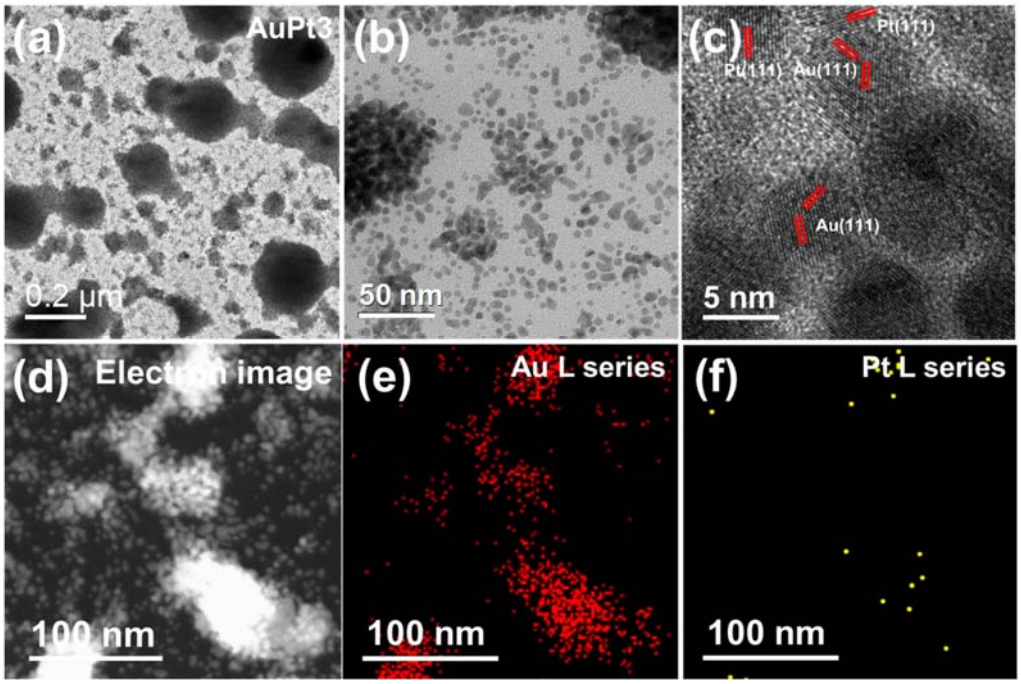

Figure S6. (a and b) TEM image and (c) HR-TEM image of the AuPt3 sample. TEM and EDX analysis results of the AuPt3 sample: (d) Electron image and EDX mapping images of (e) Au and (f) Pt elements.

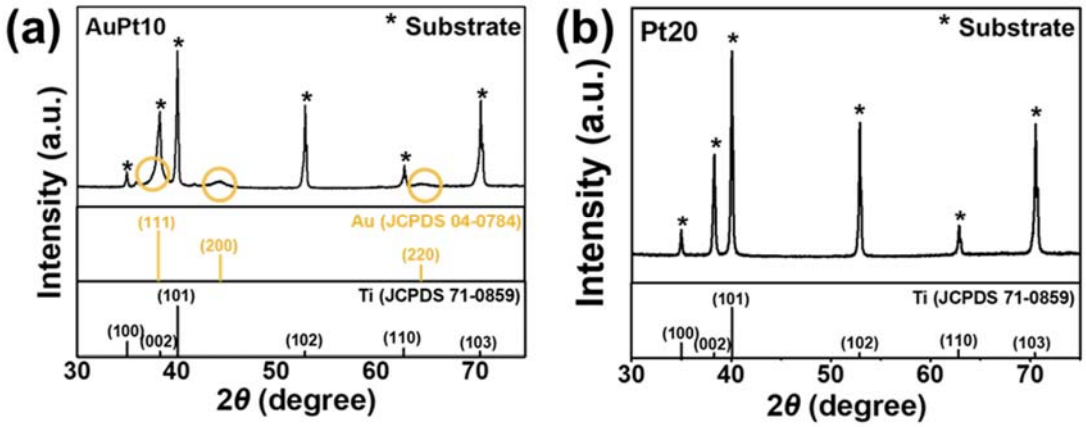

Figure S7. XRD patterns of (a) AuPt10 and (b) Pt20 samples.

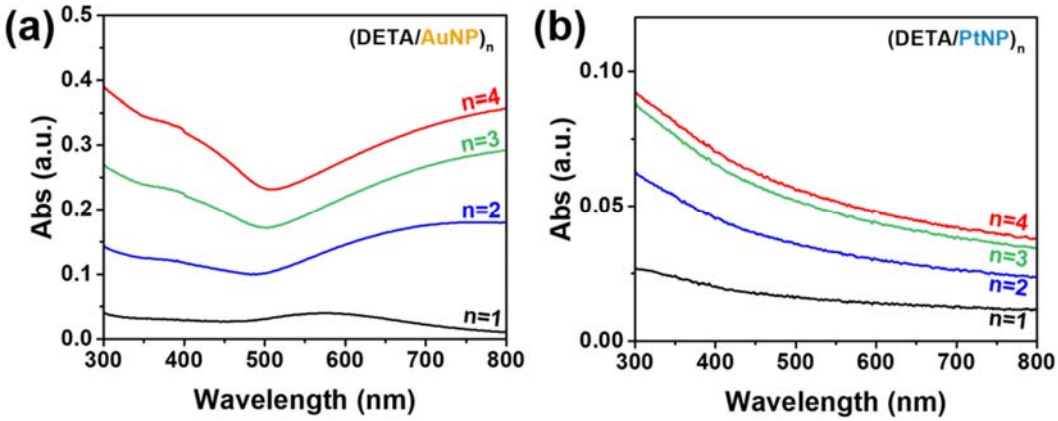

Figure S8. UV–visible absorbance spectra of (a) $(DETA/AuNP)_n$ and (b) $(DETA/PtNP)_n$ samples.

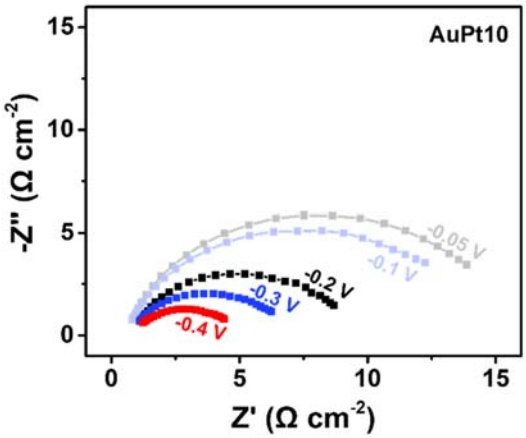

Figure S9. Electrochemical impedance spectroscopy (EIS) of AuPt10 at various overpotentials at frequency range from 100 kHz to 0.1 Hz in 0.5 M H_2SO_4.

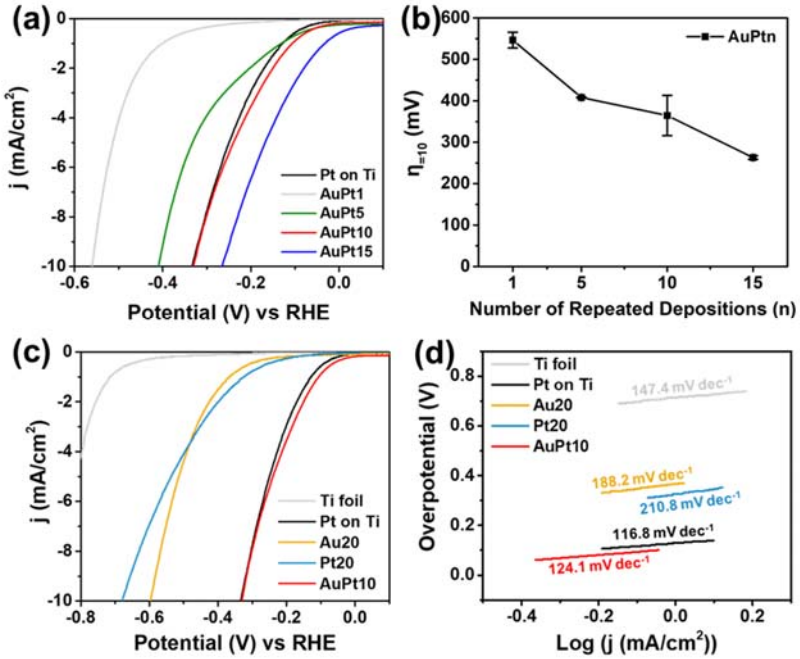

Figure S10. (a) Polarization curves of Pt sputtered onto the Ti sample and AuPtn electrodes in 1 M KOH. (b) Corresponding overpotentials at 10 mA cm^{-1}. (c) Polarization curves of the Ti substrate, Pt sputtered on Ti, Au20, Pt20, and AuPt10 electrodes in 1 M KOH. (d) Tafel slopes corresponding to (c).

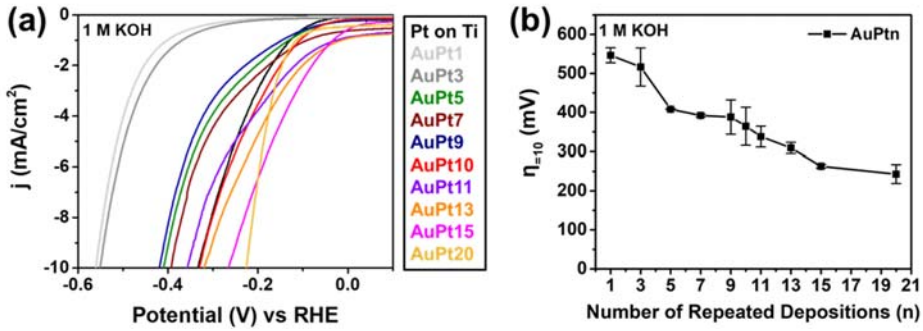

Figure S11. LSV polarization curves for AuPt*n* samples and Pt sputtered onto Ti (a) in 1 M KOH (b) Overpotentials corresponding to the curves shown in (a) at 10 mA cm^{-1}.

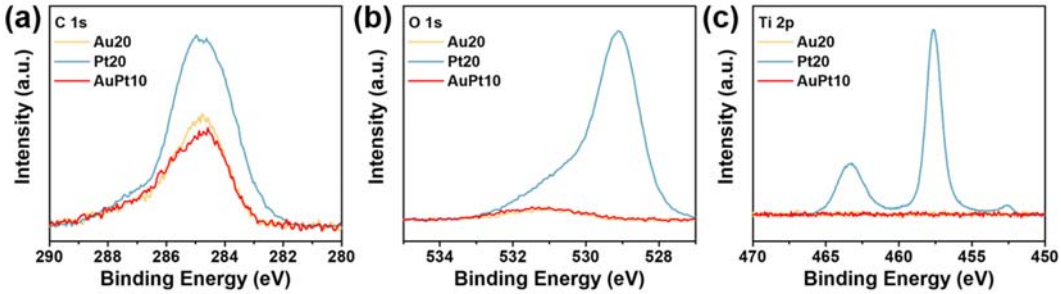

Figure S12. XPS spectra of (a) C 1s, (b) O 1s, and (c) Ti 2p peaks for Au20, Pt20, and AuPt10 samples.

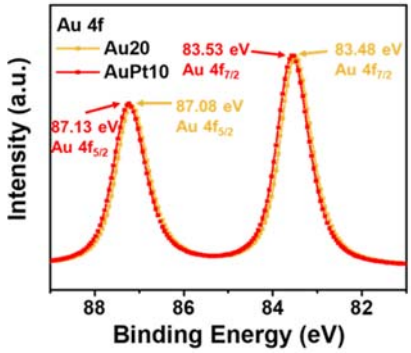

Figure S13. XPS spectra of Au 4f peaks in Au20 and AuPt10

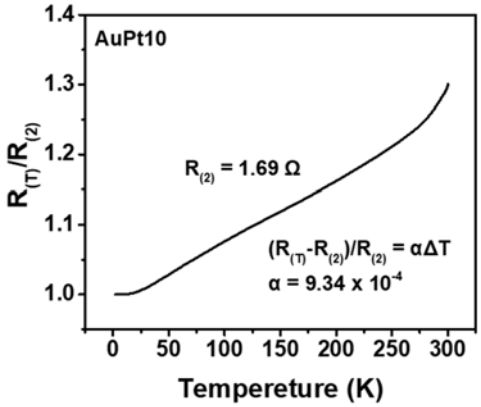

Figure S14. Resistance ($R_{(T)}/R_{(2)}$) vs temperature (K) of AuPt10 sample.

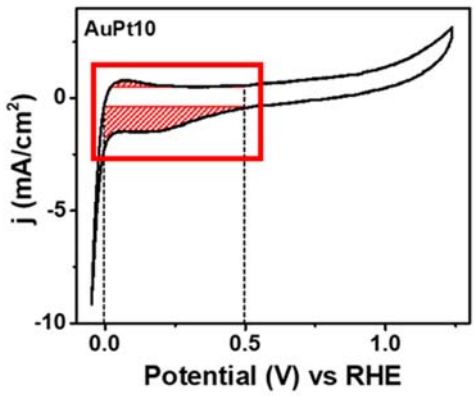

Figure S15. CV curves for ECSA of the AuPt10 electrode at scan rate of 0.5 V s^{-1} in 0.5 M H_2SO_4.

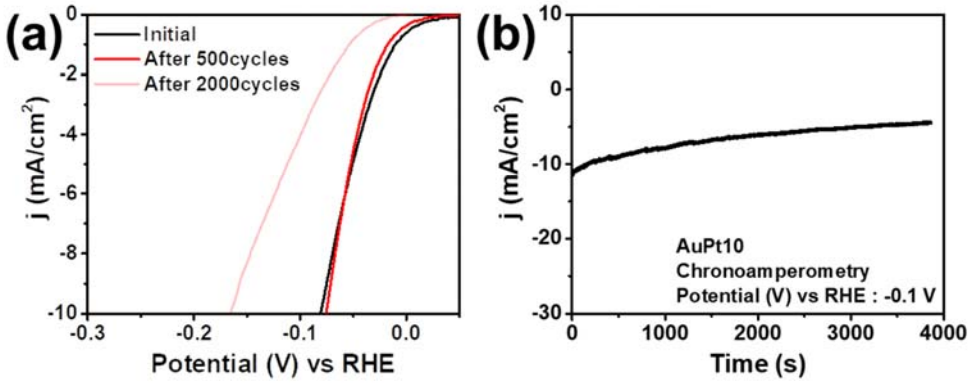

Figure S16. (a) LSV polarization curves of AuPt10 before, after 500 cycles and after 2000 cycles at scan rate of 0.5 V s^{-1} and (b) Chronoamperometry measurement of AuPt10 at an applied potential of -0.1 V vs RHE in 0.5 M H_2SO_4

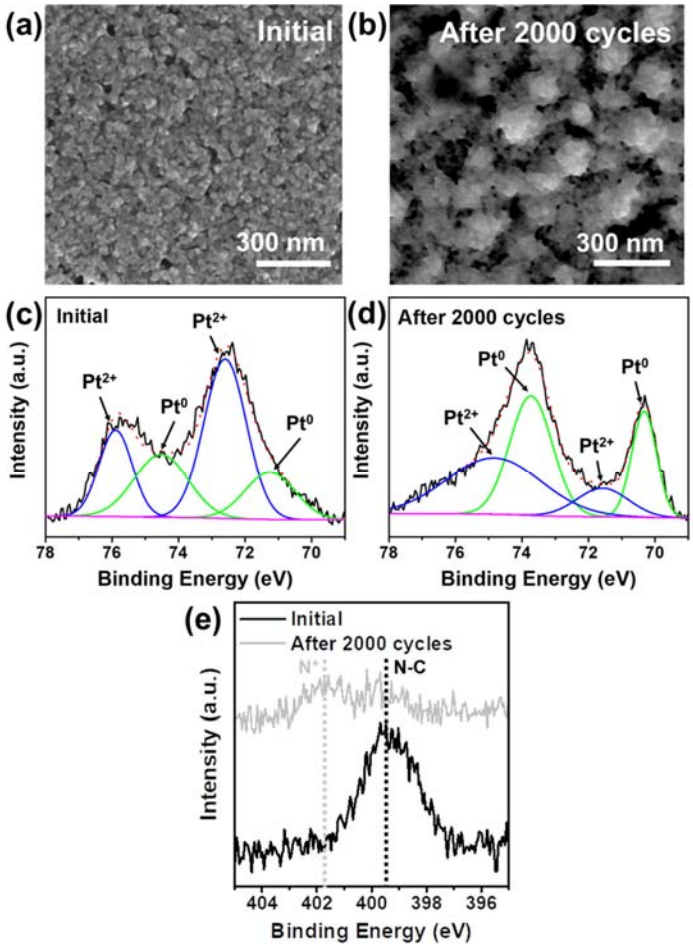

Figure S17. (a-b) FE-SEM images and XPS spectra of (c-d) Pt 4f and (e) N 1s in before and after 2000 cycles of AuPt10 at scan rate of 0.5 V s^{-1} in 0.5 M H_2SO_4.

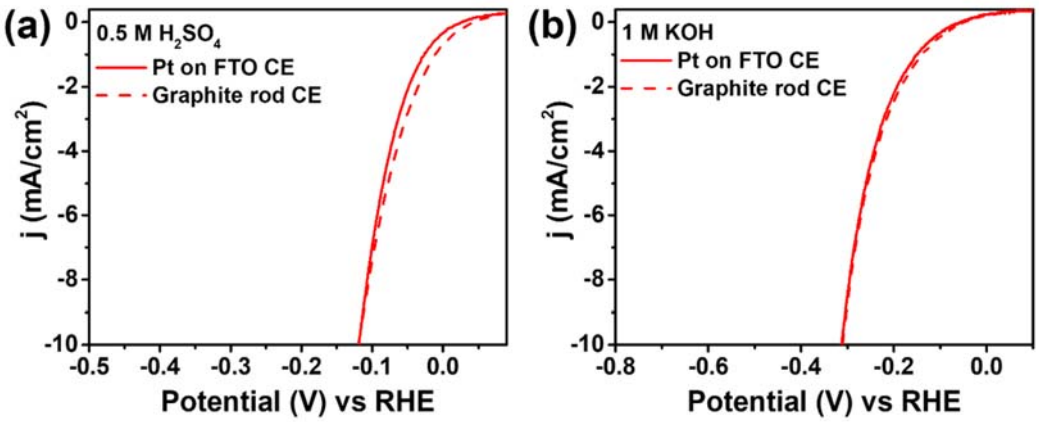

Figure S18. LSV polarization curves for AuPt10 sample at different counter electrodes in (a) 0.5 M H_2SO_4, and (b) 1 M KOH; To completely eliminate any possibility of false evaluation resulting from Pt dissolution and re-deposition, LSV was measured in the typical 3 electrode configuration using AuPt10 working electrode, Ag/AgCl reference electrode and Graphite rod counter electrode. It clearly reveals that interference of Pt counter electrode is negligible to accurately study HER performances from the AuPt*n* electrodes.

References

(S1) Yu, Y.; Lee, S. J.; Theerthagiri, J.; Fonseca, S.; Pinto, L. M. C.; Maia, G.; Choi, M. Y. Reconciling of experimental and theoretical insights on the electroactive behavior of C/Ni nanoparticles with AuPt alloys for hydrogen evolution efficiency and Non-enzymatic sensor. J. Chem. Eng 2022, 435, 134790. https://doi.org/10.1016/j.cej.2022.134790

(S2) Zhang, B.; Zhu, H.; Zou, M.; Liu, X.; Yang, H.; Zhang, M.; Wu, W.; Yao, J.; Du, M. Design and fabrication of size-controlled Pt–Au bimetallic alloy nanostructure in carbon nanofibers: a bifunctional material for biosensors and the hydrogen evolution reaction. J. Mater. Sci. 2017, 52, 8207-8218. https://doi.org/10.1007/s10853-017-1030-9

(S3) Shi, Y. C.; Chen, S. S.; Feng, J. J.; Lin, X. X.; Wang, W.; Wang, A. J. Dicationic ionic liquid mediated fabrication of Au@Pt nanoparticles supported on reduced graphene oxide with highly catalytic activity for oxygen reduction and hydrogen evolution. Appl. Surf. Sci. 2018, 441, 438-447. https://doi.org/10.1016/j.apsusc.2018.01.240

(S4) Wu, W.; Tang, Z.; Wang, K.; Liu, Z.; Li, L.; Chen, S. Peptide templated AuPt alloyed nanoparticles as highly efficient bi-functional electrocatalysts for both oxygen reduction reaction and hydrogen evolution reaction. Electrochim. Acta 2018, 260, 168-176. https://doi.org/10.1016/j.electacta.2017.11.057

(S5) Wei, Y.; Zhang, X.; Liu, Z.; Chen, H. S.; Yang, P. Site-selective modification of AgPt on multibranched Au nanostars for plasmon-enhanced hydrogen evolution and methanol oxidation reaction in visible to near-infrared region. J. Power Sources 2019, 425, 17-26. https://doi.org/10.1016/j.jpowsour.2019.03.114

(S6) Yu, B.; Liu, Q.; Nichols, F.; Mayford, K.; Pan, D.; Kuo, H. L.; Lu, J. Q.; Bridges, F. Platinum-Anchored Iron Oxide Nanostructures for Efficient Hydrogen Evolution Reaction in

Acidic Media. J. Phys. Chem. C 2023, 127, 3996–4005. https://doi.org/10.1021/acs.jpcc.2c09033.

(S7) Shan, A.; Teng, X.; Zhang, Y.; Zhang, P.; Xu, Y.; Liu, C.; Li, H.; Ye, H.; Wang, R. Interfacial Electronic Structure Modulation of Pt-MoS2 Heterostructure for Enhancing Electrocatalytic Hydrogen Evolution Reaction. Nano Energy 2022, 94, 106913. https://doi.org/10.1016/j.nanoen.2021.106913.

(S8) Dong, B.; Zhou, Y. N.; Zhou, J. C.; Ma, Y.; Yu, N.; Luan, R. N.; Dong, Y. W.; Chai, Y. M. Underpotential Deposition Promoting Low Pt Loading on MoO2/MoS2 Heterostructure towards Wide PH Green Hydrogen Evolution. Fuel 2022, 324, 124343. https://doi.org/10.1016/j.fuel.2022.124343.

(S9) Zhou, Y. N.; Liu, X.; Yu, C. J.; Dong, B.; Han, G. Q.; Liu, H. J.; Lv, R. Q.; Liu, B.; Chai, Y. M. Boosting Hydrogen Evolution through Hydrogen Spillover Promoted by Co-Based Support Effect. J. Mater. Chem. A 2023, 11, 6945–6951. https://doi.org/10.1039/D2TA09784B.